Supplementary Information

Compositional Control of Precipitate Precursors for Lithium-Ion Battery Active Materials: Role of Solution Equilibrium and Precipitation Rate

Hongxu Dong, Gary M. Koenig Jr. *

Department of Chemical Engineering, University of Virginia
102 Engineers Way
Charlottesville, VA 22904-4741

Li-ion batteries, cathode materials, high voltage spinel, transition metal oxide, precipitation.

*To whom correspondence should be addressed.
Tel: (434) 982-2714.
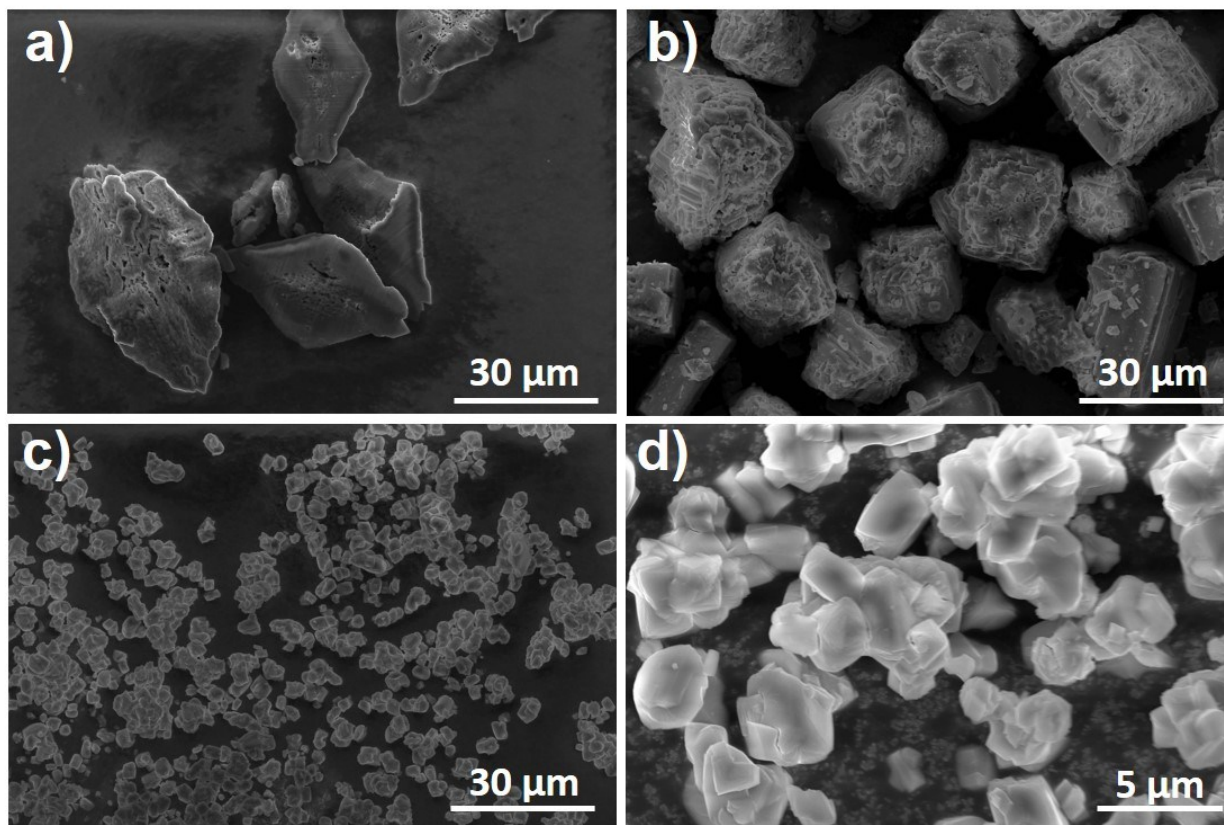Fax: (434) 982-2658.
E-mail: gary.koenig@virginia.edu

Figure S1. a) SEM image of $MnC_2O_4 \cdot 2H_2O$ collected after 30 minutes of precipitation of 20 mM Mn^{2+} feed. b) SEM image of $MnC_2O_4 \cdot 2H_2O$ used as seeds for the seeded precipitation experiments. The seeds were synthesized by collecting the precipitate after 5 minutes of precipitation of 100 mM Mn^{2+} feed. c) SEM image of $NiC_2O_4 \cdot 2H_2O$ particles collected after 30 minutes of precipitation of 20 mM Ni^{2+} feed. The SEM in d) is a higher magnification image of the same sample shown in c). In all precipitations for the particles shown in this figure, the $C_2O_4^{2-}$ feed concentration was the same as the transition metal feed concentration.
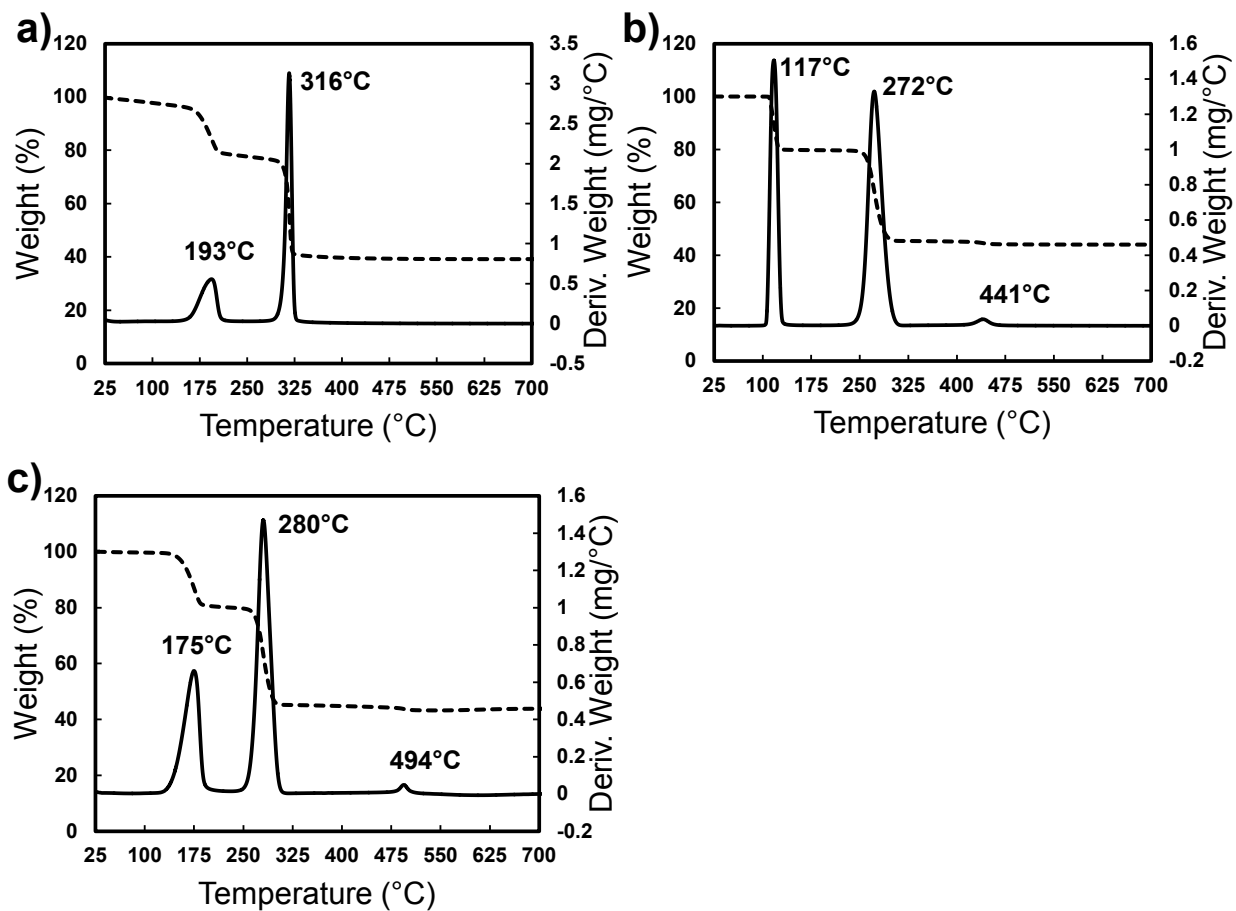
Figure S2. TGA profiles for a) $NiC_2O_4 \cdot 2H_2O$, b) $MnC_2O_4 \cdot 2H_2O$, and c) $Mn_{0.72}Ni_{0.28}C_2O_4 \cdot 2H_2O$. Dashed lines are fractional weight change as a function of temperature and solid lines are the derivative of the weight loss.

Discussion of TGA Profiles for Oxalate Precipitates

In the case of $NiC_2O_4 \cdot 2H_2O$, the dehydration was relatively gradual and peaked at 193 °C and the oxalate decomposition had a sharp peak at 316 °C (Figure S2a). The mass loss of 59.00 % was consistent with a theoretical expectation of 59.13 % for conversion to NiO. In the case of $MnC_2O_4 \cdot 2H_2O$, the dehydration peak was at 117 °C and the oxalate decomposition peak was at 272 °C (Figure S2b). The temperature for the dehydration and decomposition, as well as the further mass loss of 1% with a peak at 441 °C, were in good accordance with previous reports.[1] The final product of thermal treatment of manganese oxalate under high temperature in air is reported to be Mn_2O_3,[2–5] which was consistent with XRD patterns of our $MnC_2O_4 \cdot 2H_2O$ material heated above the minor mass loss temperature at 441 °C (data not shown). The minor mass loss has previously been attributed to the phase transition from Mn_5O_8 to Mn_2O_3, accompanied by oxygen loss and the desorption of water and carbon dioxide from the particle surface.[1,2] The total mass loss of 55.98 % was also in agreement with the theoretical value for a final product of Mn_2O_3 (55.90 %). The blend oxalate (composition $Mn_{0.72}Ni_{0.28}C_2O_4 \cdot 2H_2O$ from ICP and TGA analysis) had a dehydration peak at 175 °C and an oxalate decomposition peak at 280 °C (Figure S2c). Both peaks were between the values observed for the pure Mn and Ni oxalates. The blend oxalate had a gradual peak for dehydration, similar to that observed for the pure $NiC_2O_4 \cdot 2H_2O$. The high Mn content of the blend oxalate likely also contributes to the formation of similar Mn species that result in the small peak at higher temperatures also observed in $MnC_2O_4 \cdot 2H_2O$ samples (Figures 2b,c).
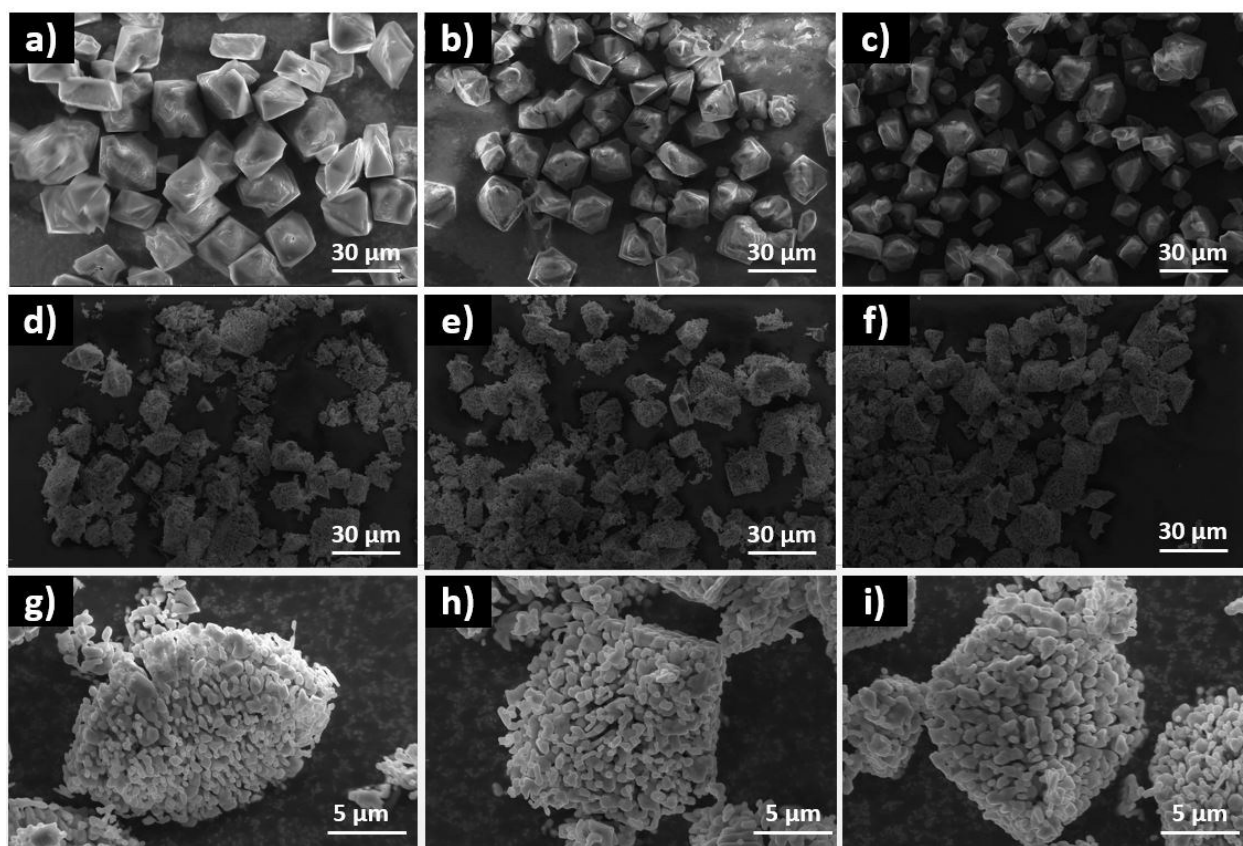
Figure S3. SEM images of a) Mn-rich, b) stoichiometric, and c) Ni-rich oxalate precursors; and the resulting d) Mn-rich, e) stoichiometric, and f) Ni-rich LMNO materials. g), h), and i) are the same powders as d), e), and f) at higher magnification.
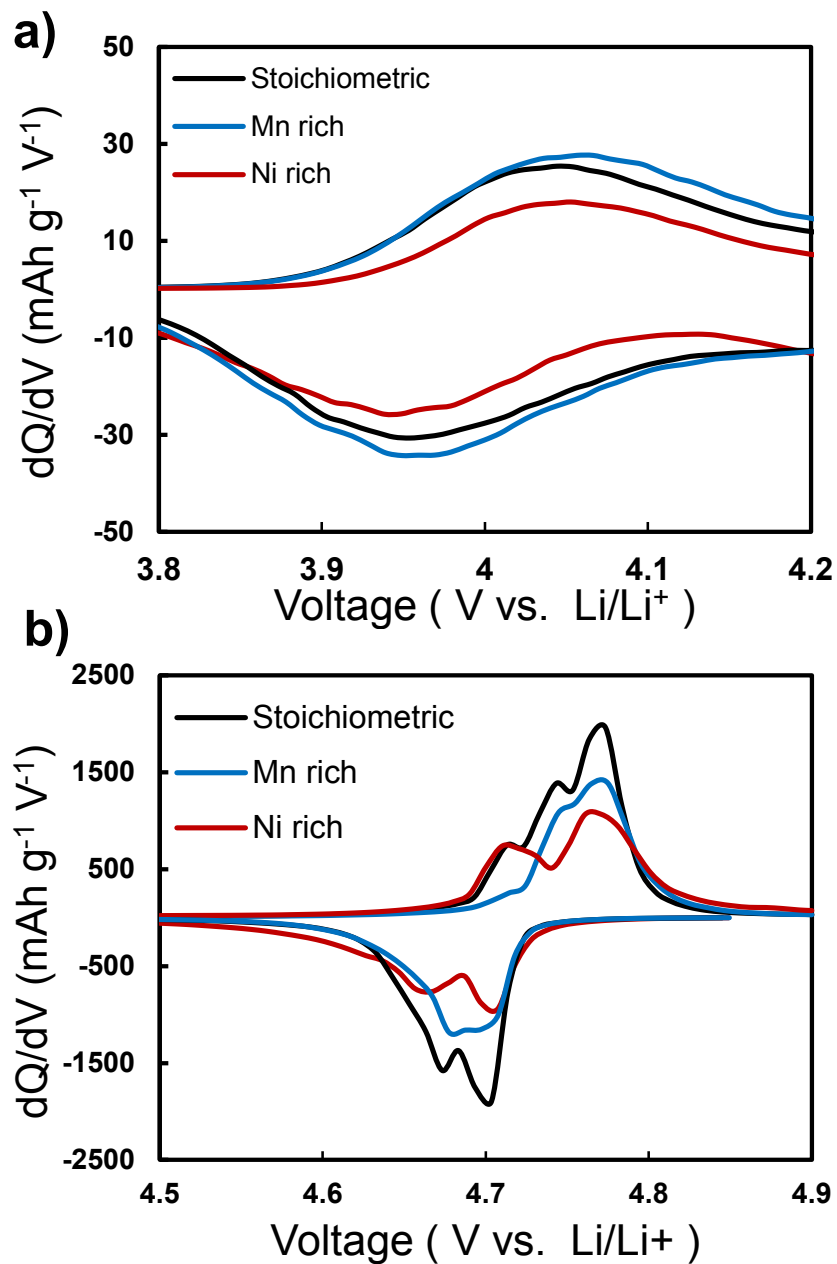
Figure S4. dQ/dV curves for the stoichiometric, Mn-rich, and Ni-rich materials cycled in Li/LMNO cells. The cells were cycled between 3.6 and 4.9 V (vs. Li/Li⁺) and the regions shown are a) 3.8 to 4.2 V and b) 4.5 to 4.9 V. The cells were cycled at a rate of C/20 (6.3 mA/g LMNO).

Discussion of dQ/dV curves for LMNO cells

Figure S4 shows the dQ/dV for the second charge/discharge cycle at rate of C/20 for the stoichiometric, Mn-rich, and Ni-rich materials. The voltage range for Figure S4a was chosen to focus on the range associated with the Mn^{3+}/Mn^{4+} redox couple and the voltage range for Figure S4b was chosen to focus on the range associated with the $Ni^{2+}/Ni^{3+}/Ni^{4+}$ redox couple(s). In the low voltage range (Figure S4a), all samples had a broad Mn oxidation peak between 4.0-4.1 V that corresponded to the low voltage capacity region during charge/discharge. The dQ/dV peak areas of the Mn-rich and stoichiometric LMNO cells were close, and both were greater than that of the Ni-rich LMNO, indicating that the Mn^{3+} content in the Mn-rich and stoichiometric LMNO was greater and consistent with other results reported in this manuscript. For the Ni redox couple peaks observed above 4.6 V (Figure S4b), three different peak positions were exhibited during Ni oxidation on charging. Kim et al. previously reported that Fd-3m disordered LMNO had two separate peaks at 4.7 V and 4.76 V in dQ/dV charging curves, while the $P4_332$ ordered LMNO structure also had two peaks but they were closer in potential at 4.74 V and 4.76 V. (6) The lower voltage peak shifted from 4.7 V to 4.74 V at the transition from the disordered to ordered LMNO while the higher voltage peak maintained the same voltage. Duncan et al. reported similar results, where the separation between the Ni oxidation peaks for dQ/dV was 20 – 30 mV for the ordered LMNO and 60 – 65 mV for the disordered LMNO. (7) Thus from the Ni oxidation peak positions of the three samples in Figure S4b, the results were consistent with the Ni-rich LMNO sample dominated by the Fd-3m disordered phase and the Mn-rich and stoichiometric LMNO samples exhibiting a blend of both the ordered and disordered spinel phases in the samples (thus both lower voltage Ni oxidation peaks were observed for three peaks in total). The results in Figure S4 were also consistent with a previous report from Zhong et al. that studied a series of different Mn:Ni

compositions; they observed a larger separation of around 60 mV for the Mn:Ni 3:1 sample that contained $Li_xNi_{1-x}O$ rock salt impurity phase, and smaller separation for the Mn-rich LMNO. (8) We also observed XRD features consistent with the rock salt impurity phase for our Ni-rich material, and thus having two observable Ni oxidation peaks for this sample with greater separation was consistent with the rock salt impurity phase inducing electrochemical features consistent with only the disordered phase in the spinel structure. We also note that high Mn^{3+} content in the structure has also been reported to result in transition from ordered to disordered spinel phase according to Duncan et al.'s report.
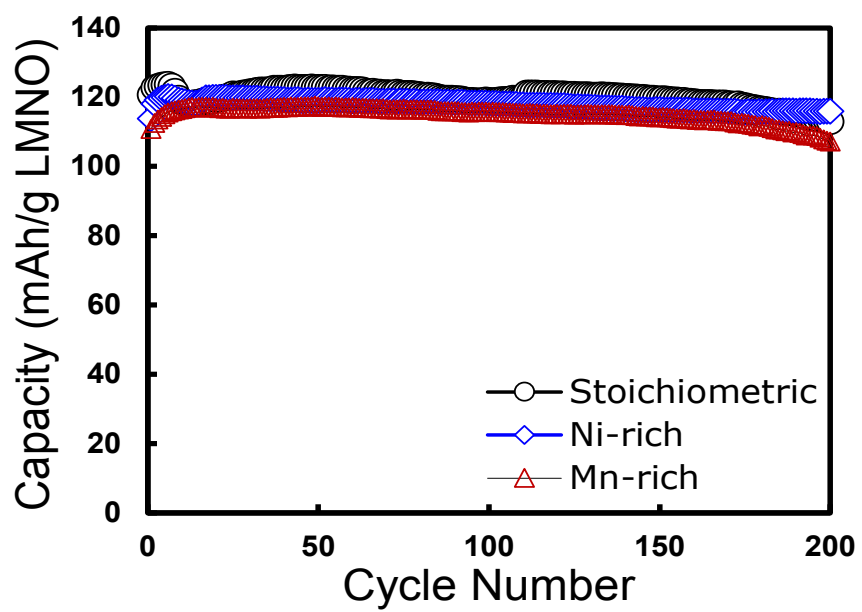
Figure S5. Cycle life test of stoichiometric (black circles), Mn-rich (red triangles), and Ni-rich (blue diamonds) LMNO. Cells were charged and discharged at C/10 rate (14.67 mA/g LMNO).

Table S1. The resulting Mn:Ni ratios precipitates formed from 3:1 Mn:Ni feed stoichiometry as a function of total initial concentration of transition metal in the feed. Values are tabulated for equilibrium calculations, ICP measurements, and the deviation between calculations and measurements.

Feed Concentration (mol/L)	Equilibrium Calculation	Measured using ICP	Deviation from Equilibrium (%)
0.10	2.88	2.97	3.13
0.05	2.76	2.86	3.62
0.02	2.38	2.71	13.9
0.01	1.72	2.33	35.5

Note: The stoichiometries measured of the precursors collected after 30 minutes were slightly different from those based on *in-situ* TM concentration measurements. This likely resulted from the processing time and washing and filtering stages completed on the final full volume of precursor solution.

Table S2. The Mn:Ni ratio in the initial feed, calculated for the resulting precipitate at equilibrium, and measured in the resulting precipitate using ICP for the Ni-rich, stoichiometric, and Mn-rich materials.

Feed Ratio	Mn:Ni Ratio in Precipitate		Deviation from Equilibrium (%)	Chemical Formula of LNMOs Measured by ICP
	Equilibrium Calculation	Measured using ICP		
3.00	2.38	2.71	13.9	$Li_{0.94}Mn_{1.46}Ni_{0.54}O_4$
3.52	2.85	3.02	5.85	$Li_{0.97}Mn_{1.50}Ni_{0.50}O_4$
3.82	3.11	3.33	7.18	$Li_{0.96}Mn_{1.54}Ni_{0.46}O_4$

Note: The resulting stoichiometry of the active material after calcination is in the final column. Li, Mn, and Ni for the final material were determined via ICP ratios, while the O was assumed to be 4.

References

1. Topfer J, Jung J. Thermal decomposition of mixed crystals NixMn3-x(C2O4)3.6H2O. Thermochim Acta. 1992;202:281–9.

2. Thota S, Prasad B, Kumar J. Formation and magnetic behaviour of manganese oxide nanoparticles. Mater Sci Eng B [Internet]. Elsevier B.V.; 2010;167(3):153–60. Available from: http://dx.doi.org/10.1016/j.mseb.2010.01.049

3. Donkova B, Mehandjiev D. Mechanism of decomposition of manganese(II) oxalate dihydrate and manganese(II) oxalate trihydrate. Thermochim Acta. 2004;421(1–2):141–9.

4. Brown ME, Galwey AK. Thermal Decomposition of Manganese(II) Oxalate in Vacuum and in Oxygen. J Chem Soc Faraday Trans 1 Phys Chem Condens Phases. 1974;70:1316–24.

5. Gao X, Dollimore D. The thermal decomposition of oxalates. Thermochim Acta [Internet]. 1993 Feb [cited 2015 Aug 12];215:47–63. Available from: http://www.sciencedirect.com/science/article/pii/004060319380081K

6. Kim J-H, Myung S-T, Yoon CS, Kang SG, Sun Y-K. Comparative Study of LiNi0.5Mn1.5O4-δ and LiNi0.5Mn1.5O4 Cathodes Having Two Crystallographic Structures: Fd 3 m and P 4332. Chem Mater [Internet]. American Chemical Society; 2004 Mar 1;16(5):906–14. Available from: http://dx.doi.org/10.1021/cm035050s

7. Duncan H, Hai B, Leskes M, Grey CP, Chen G. Relationships between Mn 3+ Content, Structural Ordering, Phase Transformation, and Kinetic Properties in LiNi x Mn 2– x O 4 Cathode Materials. Chem Mater [Internet]. 2014;26(18):5374–82. Available from: http://dx.doi.org/10.1021/cm502607v

8. Zhong Q, Bonakclarpour A, Zhang M, Gao Y, Dahn JR. Synthesis and Electrochemistry of LiNixMn2-xO4. J Electrochem Soc [Internet]. 1997;144(1):205–13. Available from: http://jes.ecsdl.org/cgi/doi/10.1149/1.1837386